aeroacoustics volume 2 · number 2 · 2003 – pages 193 – 218

Numerical evidence of mode switching in the flow-induced oscillations by a cavity

Xavier Gloerfelt, Christophe Bogey and Christophe Bailly
Laboratoire de Mécanique des Fluides et d'Acoustique
Ecole Centrale de Lyon & UMR CNRS 5509
69134 Ecully, France
e-mail: christophe.bailly@ec-lyon.fr

ABSTRACT

A Direct Noise Computation (DNC) has been performed for a turbulent boundary layer past a rectangular cavity, matching one configuration of Karamcheti[1] experiments. An LES approach with periodic boundary conditions in the spanwise direction is used to evaluate the solution at a reasonable computational cost. The two components in the pressure spectra found experimentally are well reproduced. The acoustic field appears to be dominated by the low-frequency component whereas the experimental visualization indicates a radiation at the higher frequency. The mechanism giving rise to the lower frequency is investigated providing evidence on the possibility of switching between two cavity modes and that the strong coupling of the separated shear layer with the recirculation flow within the cavity is likely to participate to the low-frequency modulation. Moreover, an extrapolation method is proposed and applied to obtain the far-field from the near acoustic field.

1 INTRODUCTION

The noise radiated by a flow past a cavity has been widely studied during the last fifty years because of its practical interest and because of the variety of theoretical questions that it raises. A complex feedback process sustains coherent oscillations in the shear layer developing above the cavity. These oscillations often take the form of Kelvin-Helmholtz rolls, whose regular impingement on the front corner of the cavity produces high-intensity periodic acoustic waves. These pressure disturbances exert a feedback influence on the selection of the shear layer instabilities. The pioneering work of Karamcheti[1] (1955) figures the externally radiated field through a Schlieren technique, and remains one of the few available measurements showing the structure of the acoustic field. This constitutes a great opportunity for the comparison with the Computational Aeroacoustics (CAA) tool. Cavity aeroacoustics is at the present time one of the most popular test case for CAA because of its geometrical simplicity. The numerical investigation tool can help toward a better understanding of the noise generation mechanisms. The first 2-D CAA approaches[2–5] using Direct Numerical

Simulation (DNS) of the full compressible Navier-Stokes equations have demonstrated the feasibility of computing the frequency peaks and the structure of the radiated field. The strong upstream directivity agreed well with the visualisations of Karamcheti. The numerical constraints imposed by the DNS approach have limited these simulations[2–5] to bidimensional, small-dimension, and high-speed configurations. The comparison with the Karamcheti experiments using various length-to-depth ratios for rectangular cavities with a fixed 0.1 inch depth, spanning the transverse dimension of the wind tunnel, and with freestream Mach numbers between 0.4 and 0.8, seemed therefore natural. Another interesting issue in Karamcheti's study is the different behaviour observed depending on whether a laminar or a turbulent boundary layer interacts with the cavity, the aspect ratio and the stream velocity being kept constant. The frequency of the oscillations for a turbulent inflow is slightly lower than the one measured with a laminar inflow. Moreover, a low frequency appears in the spectra for a turbulent inflow. The origin of this low-frequency component, with roughly half the frequency of the fundamental, remains unexplained. Is it a subharmonic, a modulation of the impingement event, the presence of a lower mode during the dominant mode, or an intermittent or deterministic switching between two competitive cavity modes of oscillations?

The aim of this study is to use the numerical simulation, and its powerful analysis capacity, to reproduce and characterize this low-frequency phenomenon. Intermittency of the shear-layer turbulence may lead to the multiple modes which apparently coexist. This conjecture[6] has however few clear experimental illustrations. An alternance between modes, called *mode-switching* is for instance observed in the experiments of Cattafesta *et al.*[7] The fact that the vortices are rather clusters of small scales than single rolls in fully turbulent shear layers, *i.e.* at high Reynolds numbers, may play a determinant role.

In an earlier work,[8] a laminar configuration of Karamcheti's experiments was successfully reproduced for a cavity length-to-depth ratio $L/D = 2$, by using 2-D DNS. This reference solution has allowed the detailed comparison with three integral formulations to compute the acoustic far-field. However, the 2-D simulations are limited to thick incoming boundary layer in order to avoid a bifurcation toward a so-called *wake mode*, where the dynamics of the shear layer is overwhelmed by the recirculating flow inside the cavity. This numerical artefact arises from the non-mixing of contrarotative vortices in a 2-D plane. A 3-D approach is required to reproduce the dynamics of the recirculation. Moreover, the simulation of a realistic turbulent boundary layer is necessarily three-dimensional. A DNS solving all the scales (down to the Kolmogorov scale) becomes impractical in 3-D, and must be replaced by a method using turbulent modellings. The first one is Large Eddy Simulation (LES) where only the structures discretised by the meshgrid are computed, using the fact that the cavity flow is dominated by the interactions of coherent structures with the downstream corner.[9,10] Larchevêque *et al.*[9] performed LES of the 3-D flow over a $L/D = 0.42$ cavity at a Mach number of 0.8, and a Reynolds number $\mathrm{Re}_L = 8.6 \times 10^5$. Their results compare remarkably well with the corresponding experimental measurements by Forestier *et al.*[11] For high-Reynolds number flows, Shieh and Morris[12] proposed the use of a hybrid RANS/LES approach based on the Detached Eddy Simulation (DES) concept. This method aims at exploiting the best features of both approaches by

solving RANS in the turbulent boundary layer and a one-equation LES in the separated shear layer.

In the present study, a 3-D LES is performed for the moderate Reynolds number considered in order to describe the behaviour of the small scales and the intermittency of the turbulence. The effects of the unresolved subgrid scales are modelled via the Smagorinsky eddy viscosity with a self-adaptive Van Driest damping function near the solid boundaries. The influence of this model and of the choice of the Smagorinsky constant are discussed in the case of the development of a turbulent boundary layer. The efficiency of the model in the separated shear layer above the cavity is only briefly addressed, since no aerodynamic measurement is available for this configuration. The standard Smagorinsky model is seen to be often too dissipative in high Reynolds number flows.[13] It can be inferred that the eddy viscosity may have a non-negligible effect on the shear layer dynamics, and that a less dissipative model would be helpful to preserve high Reynolds number features.

Another modelling issue concerns the prescription of a realistic turbulent boundary layer ahead of the cavity. Perturbations are superimposed on an initial turbulent profile in the inlet plane in order to bypass transition, and accelerate the eruption of true turbulence ahead of the cavity. A turbulent boundary layer with zero pressure gradient is simulated to check the rapid spatial development of realistic turbulence.

Since most of the previous turbulent boundary layer simulations used periodic boundary conditions in the spanwise direction, and also to account for the very large length-to-width ratio in the Karamcheti experiment, the lateral boundary conditions are assumed periodic for the flow. Only a slice of the physical domain is computed, reducing the numerical cost. This assumption is physically justified since the main features of cavity flows are found to be bidimensional for length-to-width ratios $L/W < 1$, as shown by Ahuja and Mendoza.[14] The 3-D character of the simulation is necessary to describe the turbulent mixing but a high degree of coherence is observed in the spanwise direction.

Despite the grid limitation, a large range of length and time scales are still involved, from the small structures of the turbulent boundary layer to the long wavelengths of the acoustic waves. To cope with this, the computational domain is often truncated in an acoustic region not too far beyond the unsteady flow. A simple method must then be applied to extend the acoustic near-field from the cavity Direct Noise Computation (DNC) to the far-field in order to ensure that cancellations and superpositions that may occur in the acoustic region do not change the structure of the far-field. Several numerical methods for extending the sound field have been proposed. One approach is to use wave equation solutions formulated as a surface integral such as the Kirchhoff or Ffowcs Williams and Hawkings Wave Extrapolation Methods which have been applied to jet[15,16] or cavity simulations.[8] The far-field solution is then expressed as a single integral, reducing the computational requirements. This is particularly convenient when only a directivity using few sensors is needed. Nevertheless, the integral formulations require data for all the retarded times from sound emission until reception. When the source region is very extended, the temporal storage needed to evaluate the integral solution is large. These methods become hardly practical due to computer memory limitations. Moreover the integral methods assume an acoustic medium with constant

properties, so that they cannot deal with nonlinear propagation. Another solution, proposed by Freund *et al.*[17] or Shih *et al.*,[18] consists in matching the Navier-Stokes solver to a far-field region where a wave equation or a similar set of acoustic equations are solved. The implementation is simpler since the data are now only needed sequentially. The matching should allow for two-way communication between the domains. In the present work, to avoid the matching region necessary for transferring informations from the acoustic grid to the DNC grid, a slightly different method is proposed. The DNC is made independent of the extrapolation method by using two grids with different boundary conditions. The acoustic solver is thus easier to couple with the DNC since no transfer from the coarse grid to the fine grid is needed, allowing the use of a much larger meshsize and time step in the acoustic calculation.

The paper is organised as follows. In the first part, the numerical methods used for the 3-D Direct Noise Computation of cavity aeroacoustics are described. The second part presents the results of the simulation for the $L / D = 3$, $\mathrm{M} = 0.8$ turbulent configuration of Karamcheti's experiments.[1] The switching between two cavity modes is demonstrated.

2 NUMERICAL METHODS FOR THE DIRECT NOISE COMPUTATION

2.1 Governing equations

3-D filtered Navier-Stokes equations for compressible fluids

A schematic view of the flow domain is shown in figure 1. The origin of the coordinate system is located at the middle of the upstream corner. For the Direct Noise Computation, the full three-dimensional compressible Navier-Stokes equations are solved to simulate both the flow and the acoustic perturbations. They are expressed in a conservative form in the Cartesian coordinate system of figure 1. In Large Eddy Simulation, only the scales larger than the grid size are computed explicitely, and the subgrid scales are modelled. The governing equations are obtained after spatial filtering, denoted by a bar. The velocity components are decomposed into a resolved part, $\tilde{u}_i = \overline{\rho u_i} / \overline{\rho}$, using Favre averaging, and an unresolved part, u_i''. The resulting system solved in the present study is:

$$\frac{\partial \mathbf{U}}{\partial t} + \frac{\partial \mathbf{E_e}}{\partial x_1} + \frac{\partial \mathbf{F_e}}{\partial x_2} + \frac{\partial \mathbf{G_e}}{\partial x_3} - \frac{\partial \mathbf{E_v}}{\partial x_1} - \frac{\partial \mathbf{F_v}}{\partial x_2} - \frac{\partial \mathbf{G_v}}{\partial x_3} = 0 \tag{1}$$

with:

$$\mathbf{U} = (\overline{\rho}, \overline{\rho}\tilde{u}_1, \overline{\rho}\tilde{u}_2, \overline{\rho}\tilde{u}_3, \overline{\rho}\tilde{e})^t$$

$$\mathbf{E_e} = (\overline{\rho}\tilde{u}_1, \overline{p} + \overline{\rho}\tilde{u}_1{}^2, \overline{\rho}\tilde{u}_1\tilde{u}_2, \overline{\rho}\tilde{u}_1\tilde{u}_3, (\overline{\rho}\tilde{e} + \overline{p})\tilde{u}_1)^t$$

$$\mathbf{F_e} = (\overline{\rho}\tilde{u}_2, \overline{\rho}\tilde{u}_2\tilde{u}_1, \overline{p} + \overline{\rho}\tilde{u}_2^2, \overline{\rho}\tilde{u}_2\tilde{u}_3, (\overline{\rho}\tilde{e} + \overline{p})\tilde{u}_2)^t$$

$$\mathbf{G_e} = (\overline{\rho}\tilde{u}_3, \overline{\rho}\tilde{u}_3\tilde{u}_1, \overline{\rho}\tilde{u}_3\tilde{u}_2, \overline{p} + \overline{\rho}\tilde{u}_3{}^2, (\overline{\rho}\tilde{e} + \overline{p})\tilde{u}_3)^t$$

$$\mathbf{E_v} = (0, \tilde{\tau}_{11} + \mathcal{T}_{11}, \tilde{\tau}_{12} + \mathcal{T}_{12}, \tilde{\tau}_{13} + \mathcal{T}_{13}, \tilde{u}_i(\tilde{\tau}_{1i} + \mathcal{T}_{1i}) - \tilde{q}_1 - c_v\mathcal{Q}_1)^t$$

$$\mathbf{F_v} = (0, \tilde{\tau}_{21} + \mathcal{T}_{21}, \tilde{\tau}_{22} + \mathcal{T}_{22}, \tilde{\tau}_{23} + \mathcal{T}_{23}, \tilde{u}_i(\tilde{\tau}_{2i} + \mathcal{T}_{2i}) - \tilde{q}_2 - c_v\mathcal{Q}_2)^t$$

$$\mathbf{G_v} = (0, \tilde{\tau}_{31} + \mathcal{T}_{31}, \tilde{\tau}_{32} + \mathcal{T}_{32}, \tilde{\tau}_{33} + \mathcal{T}_{33}, \tilde{u}_i(\tilde{\tau}_{3i} + \mathcal{T}_{3i}) - \tilde{q}_3 - c_v\mathcal{Q}_3)^t$$

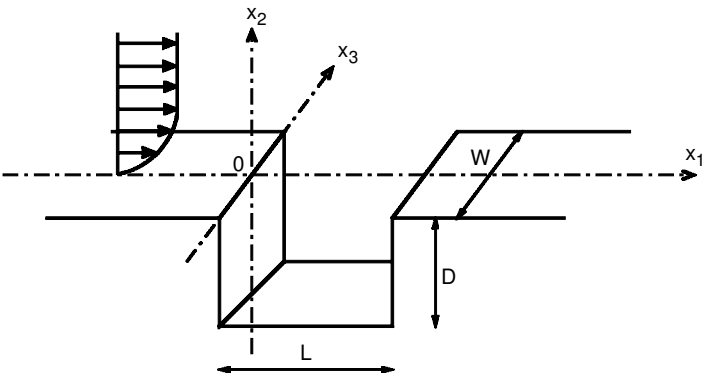

Figure 1. Sketch of the flow domain and coordinate system.

where c_v is the specific heat at constant volume. The quantities $\overline{\rho}$, $\overline{p}$, $\tilde{u}_i$ are the resolved density, pressure, and velocity components. For a perfect gas, the total energy per mass unit $\tilde{e}$ is defined as:

$$\tilde{e} = \overline{p} \,/\, [(\gamma - 1)\overline{\rho}] + (\tilde{u}_1{}^2 + \tilde{u}_2{}^2 + \tilde{u}_3{}^2)/2, \qquad \text{and} \qquad \overline{p} = r\overline{\rho}\tilde{T},$$

where $\tilde{T}$ is the temperature, r the gas constant, and γ the ratio of specific heats. The viscous stress tensor $\tilde{\tau}_{ij}$ is modelled as a Newtonian fluid $\tilde{\tau}_{ij} = 2\mu\tilde{S}_{ij}$, where μ is the dynamic molecular viscosity, and $\tilde{S}_{ij}$ the deviatoric part of the resolved deformation stress tensor:

$$\tilde{S}_{ij} = \frac{1}{2}\left(\frac{\partial\tilde{u}_i}{\partial x_j} + \frac{\partial\tilde{u}_j}{\partial x_i} - \frac{2}{3}\delta_{ij}\frac{\partial\tilde{u}_k}{\partial x_k}\right)$$

The heat flux component $\tilde{q}_i$ models thermal conduction in the flow with Fourier's law $\tilde{q}_i = -(\mu c_P/\sigma)(\partial\tilde{T}/\partial x_i)$, where σ is the Prandtl number, and c_p the specific heat at constant pressure.

Subgrid-scale modelling

The effects of the subgrid scales are present in system (1) through the subgrid scale stress tensor $\mathcal{T}_{ij}$ and the subgrid scale heat flux $\mathcal{Q}_i$, respectively:

$$\mathcal{T}_{ij} = -\overline{\rho}(\tilde{u}_i\tilde{u}_j - \tilde{u}_i\tilde{u}_j), \qquad \mathcal{Q}_i = \overline{\rho}(\tilde{u}_i T - \tilde{u}_i\tilde{T})$$

A simple closure model consists in reproducing the dissipative effets of the unresolved scales by implementing a turbulent viscosity μ_t, a subgrid scale energy k_{sgs}, and a turbulent Prandtl number σ_t. The subgrid scale tensor and heat flux can then be modelled by:

$$\mathcal{T}_{ij} = 2\mu_t\tilde{S}_{ij} - \frac{2}{3}\overline{\rho}k_{sgs}\delta_{ij}, \qquad \text{and} \qquad \mathcal{Q}_i = -\frac{\mu_t}{\sigma_t}\frac{\partial\tilde{T}}{\partial x_i}$$

We choose the Smagorinsky eddy-viscosity model, where $\mu_t = \overline{\rho}(C_S\Delta_c)^2\sqrt{2\,\tilde{S}_{ij}\,\tilde{S}_{ij}}$, C_S is the Smagorinsky constant, and $\Delta_c = (\Delta x_1 \Delta x_2 \Delta x_3)^{1/3}$ the characteristic length scale. Values of approximately $C_S = 0.1$ are typically used for wall-bounded flow.[19] The sensitivity to this choice is discussed in paragraph 2.3. The subgrid scale energy k_{sgs} is not directly available, but, following Erlebacher *et al.*,[20] it is modelled as $k_{sgs} = 2C_I\overline{\rho}\Delta_c^2\,\tilde{S}_{ij}\,\tilde{S}_{ij}$, where $C_I \simeq 0.1$. Lastly, the turbulent Prandtl number is taken constant, $\sigma_t \simeq 0.1$. In the following, the tilde notation is omitted since only resolved quantities are studied.

Wall model

One of the major drawback of the previous modelling is that the Smagorinsky model is not able to describe the scale reduction that occurs near the solid walls. A solution consists in superimposing an empirical wall law for μ_t near the solid boundaries. Moin et Kim[21] and several authors propose to weight the characteristic length scale Δ_c by the exponential van Driest damping function:

$$\Delta_c^{'} = \left\{1 - \exp\left(\frac{x_2^+}{A^+}\right)\right\}\Delta_c$$

where $A^+ = 25$ and $x_2^+ = x_2 u_\tau/\nu$ is the normal wall coordinate. The friction speed u_τ is determined by solving the logarithmic law for every point on the walls:

$$\frac{\overline{u_1}(x_1, x_2)}{u_\tau(x_1)} - 5.75\log\left(\frac{x_2 u_\tau(x_1)}{\nu}\right) + 5.24 = 0$$

with $\overline{u}_1$ designing the mean longitudinal velocity and ν the kinematic viscosity.

2.2 Algorithm and boundary conditions

Algorithm

The convective terms of (1) are integrated in time using an explicit low-storage six-step Runge-Kutta scheme optimised in the wave number space. Because of their slower time evolution, the viscous terms are only integrated in the last substep. The gradients are solved on a rectangular slowly nonuniform grid by using optimised finite-differences for an eleven-point stencil for the convective fluxes, and standard 4^{th} order finite differences for the viscous and heat fluxes. As part of the algorithm, a selective filtering built up on an eleven-point stencil is incorporated in each direction to eliminate grid-to-grid unresolved oscillations. The coefficients of the Runge-Kutta algorithm, of the finite differences and of the filtering are given in Bogey and Bailly.[22]

Solid walls

On all solid boundaries, the no-slip conditions $u_1 = u_2 = u_3 = 0$ are imposed, with $\partial p / \partial n = 0$, where n is the direction normal to the solid surface. The finite-difference

stencil for the convective terms is progressively reduced down to the fourth order. The viscous stress terms are evaluated from the interior points by using fourth order backward differences. The wall temperature is calculated with the adiabatic condition. For the sharp corners formed by the intersection of planar cavity surfaces, the variables are determined by using the interior scheme, thereby avoiding any ambiguity regarding the normal direction.

Radiation conditions

At the upstream and upper boundaries of the computational domain, the radiation boundary conditions of Tam and Dong,[23] using a far-field solution of the sound waves, are applied. The origin of the acoustic waves is located at the downstream corner, ($x_1 = L$, $x_2 = 0$, $x_3 = 0$). It must be noted that the exact location of the sound source is not very important if the boundaries are sufficiently far from the sources.[24] However, the choice of a vertical location at $x_2 = 0$ is well-suited to the implementation of the inflow and outflow boundary conditions near the walls. At the outlet, the outflow boundary conditions of Tam and Dong, where the radiation solution is modified to allow the exit of vortical and entropic disturbances, is combined with a sponge zone dissipating vortical structures. This sponge zone uses grid stretching and a progressively applied Laplacian filter.

Lateral boundaries

When the cavity span is smaller than the width of the computional domain, the sidewalls can be modelled by using the wall condition. But to account in the present simulation for the very large length-to-width ratio used in the Karamcheti experiment ($L / W = 0.03$), periodic boundary condition are applied for the lateral boundaries.

2.3 Generation of a spatial turbulent boundary layer

Most of the earlier computations of turbulent boundary layers has been limited to temporal simulations based on the quasi-periodicity of the flow in the streamwise direction. For spatially evolving boundary layers, needed in the present work, the computational region must include both the transition region and the turbulent region, and requires far greater computational resources. The three-dimensional simulation of the natural transition of a flat-plate boundary layer has only become possible recently.[25,26] A high level of accuracy is required in order to reproduce the development of Tollmien-Schlichtling waves and their breakup through secondary and tertiary instabilities. It is obviously too expensive for the present investigation since the attention is primarily focused on the interactions with the cavity. A bypass transition appears more appropriate. Voke & Yang[27] show for instance that since the transition is thus early and short, the detailed computation of the instabilities is not crucial. In the present work, an initial turbulent mean profile is used to accelerate the eruption of developed turbulence ahead of the cavity.

To create unsteady, stochastic inlet conditions, we use a synthetic flowfield, based on Random Fourier Modes (RFM).[28] The turbulent inlet field is generated as the sum

of N independent RFM, with amplitudes $\hat{u}_n$ determined from the turbulent kinetic energy spectrum. The fluctuating velocity field is then expressed as a Fourier series:

$$\mathbf{u}'(\mathbf{x},t) = \sum_{n=1}^{N} \hat{u}_n \cos(\mathbf{k}_n.(\mathbf{x} - \overline{\mathbf{u}}t) + \omega_n t + \psi_n)\mathbf{a}_n$$

where ψ_n, $\mathbf{k}_n$, $\mathbf{a}_n$ are random variables with given probability density functions. An unfrozen turbulent field is obtained by incorporating the convection velocity $\overline{\mathbf{u}}$ and the pulsation ω_n, accounting for the temporal evolution of the perturbations. In the present turbulent simulation, $N = 200$ and ω_n is deduced from the Heisenberg time, $\omega_n = 2\pi u' k_n$, where u' is the *rms* fluctuating velocity and k_n the wave number.

The turbulent boundary layer with zero pressure gradient is first chosen as a fundamental testcase to study the development of a realistic turbulent inflow. Based on DNS and LES of the literature, the size of the computational domain is taken equal to $114\delta^*$ in the streamwise direction and $25\delta^*$ in the vertical direction, δ^* being the displacement thickness given below. The spanwise extent is $28\delta^*$, with periodic boundary conditions. The Cartesian meshgrid is $201 \times 91 \times 121$ points, with constant spacings in the x_1 and x_3 directions, and 3% stretching in the x_2-direction. The grid spacings in wall units, nondimensionalised by ν/u_τ, are $\Delta x_1^+ = 50$, $\Delta x_{2_{min}}^+ = 5$, and $\Delta x_3^+ = 20$, where $u_\tau = 7.8$ m/s is obtained from the logarithmic law. The Mach number of the flow is 0.5. The simulation is initialised with the mean profile $\overline{u}_1(x_2)$ from Spalart's[29] temporal boundary layer simulation at $\mathrm{Re}_{\delta_\theta} = 1410$ extrapolated into the entire computational domain. The stochastic turbulent field, generated by the method described above, is weighted by the vertical profiles of *rms* velocities from Spalart's[29] temporal DNS, and is superimposed on the mean profile. Tam and Dong's radiation boundary conditions are applied on the free boundaries. 30000 temporal iterations are performed with $\Delta t \simeq 2 \times 10^{-8}$ s, and C_S is taken equal to 0.1.

Figure 2 shows contours of the calculated vorticity. The onset of realistic turbulence is seen to occur roughly after $50\delta^*$ in the streamwise direction. The flow structure has then similarities with the results of Spalart or with experimental smoke pictures.[30] In the region where the boundary layer is estimated to be fully established, at $x_1 = 62\delta^*$, the boundary layer thickness is $\delta = 1.26 \times 10^{-3}$m, the displacement thickness is $\delta^* = 1.75 \times 10^{-4}$ m, and the momentum thickness $\delta_\theta = 1.23 \times 10^{-4}$ m, giving a shape factor $H = \delta^*/\delta_\theta = 1.42$. The Reynolds number based on the momentum thickness is $\mathrm{Re}_{\delta_\theta} = 1410$. Spalart[29] gives $H = 1.42$ for $\mathrm{Re}_{\delta_\theta} = 1410$. To demonstrate that a log layer exists within the turbulent boundary layer, the longitudinal mean velocity $\overline{u}_1^+ = \overline{u}_1/u_\tau$ is plotted on semilog coordinates in figure 3(a). A well-defined log region is visible even if the viscous sublayer is not resolved by the meshgrid used. Moreover, to ascertain that a inertial subrange exists, spectra of the kinetic energy are evaluated at a distance 0.5δ from the wall, for $x_1 = 62\delta^*$, and averaged over 7 locations in the homogeneous spanwise direction. The spectra used 2000 samples of the velocity fluctuations recorded every 10 temporal iterations. The energy spectrum of figure 3(b) shows the typical $-5/3$ law in the inertial subrange.

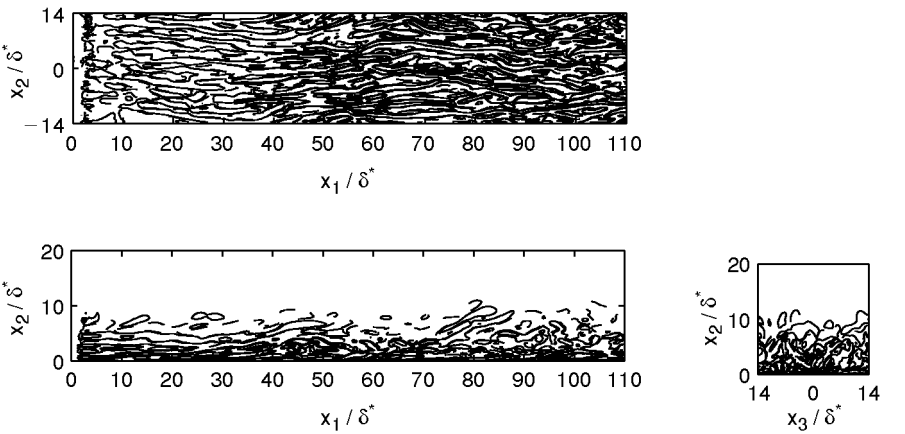

Figure 2. Turbulent boundary layer testcase. Vorticity isocontours: topview of ω_{13} at $x_2 = 0.6\delta*$, sideview of ω_{12} at $x_3 = 0$, and crossview of ω_{23} at $x_1 = 86\delta*$. (——): positive contours $[0.1;1;10]\times 10^5$; (– – –) : negative contours $[-10;-1;-0.1]\times 10^5$.

An important question regards the influence of the choice of the Smagorinsky constant on the flow dynamics. Figure 4 shows the vertical variation of the turbulence intensities obtained for three values of C_S: the standard value of 0.18 for isotropic turbulence, the value of 0.1 commonly used for wall-bounded flow, and a lower value of 0.02. Comparison of these distributions with those of Spalart's simulation[29] indicates

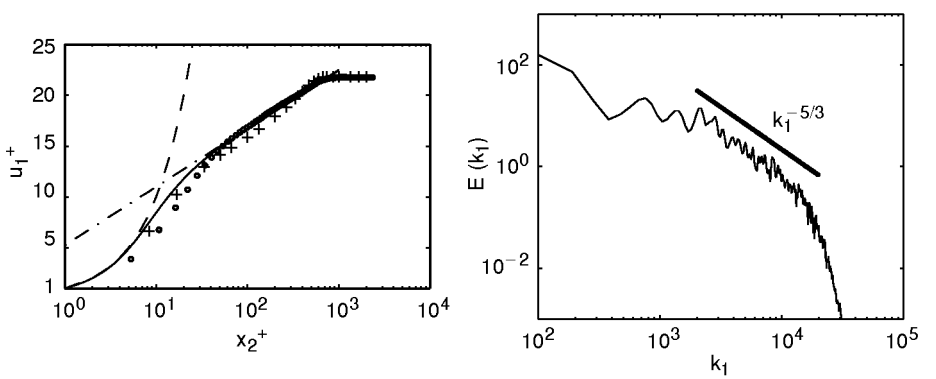

Figure 3. Turbulent boundary layer testcase. Mean profile of $\overline{u}_1/u_\tau$ (a): (∘ ∘), present LES; (++), Spalart's DNS[29]; (– – –), linear law; (– . – .), logarithmic law; (——), analytical Van Driest profile. Energy spectrum of vertical velocity fluctuations (b) in the boundary layer at a distance of 0.5δ from the wall.

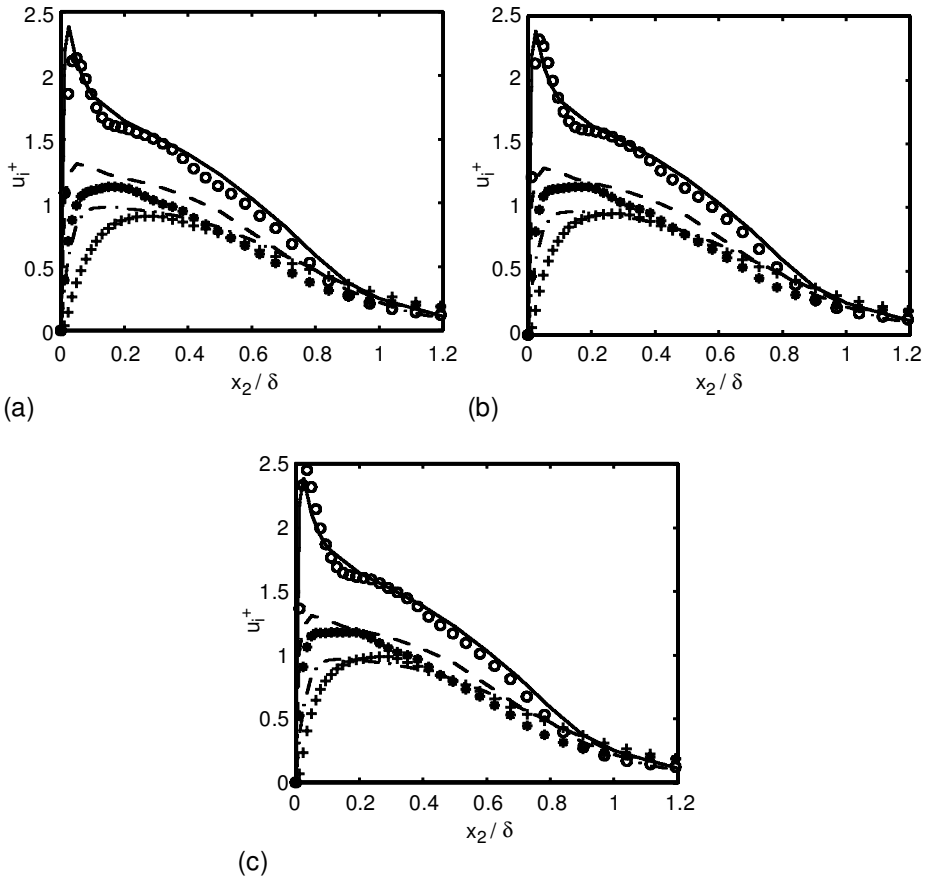

Figure 4. Turbulent boundary layer testcase. Turbulent intensities for the spatial LES (symbols) and the temporal DNS of Spalart[29] (lines): ($\circ\circ$,——), u_{1rms}/u_τ; (++, – . – .), u_{2rms}/u_τ; (**, – – –) u_{3rms}/u_τ. Three values of the Smagorinsky constant are tested: $C_s = 0.18$ (a), $C_s = 0.1$ (b), and $C_s = 0.02$ (c).

fairly good agreement for all cases. The only slight differences are seen near the solid walls with larger gradients for smaller values of the constant. The weak sensitivity to the value of C_S indicates that the turbulent boundary layer is well resolved by the present numerical method. The use of high-order schemes, such as those optimised by Bogey and Bailly,[22] is seen to be crucial with the aim of computing accurately the resolved scales by LES because of their low intrinsic numerical dissipation. It was particularly shown that since the filtering affects only the short waves discretised by less than four grid points, the features of the resolved scales are independent on this artificial energy-dissipating process.[31]

The main features of the spatial development of a turbulent boundary are thus satisfactorily reproduced by using RFM to bypass the transition. The multiplication of the stochastic velocity by given vertical profiles of *rms* velocities ensures a shorter transitional region but has two drawbacks. First, the incompressibility condition is no longer ensured and the excitation becomes noisy, but this spurious radiation is however sufficiently weak compared to cavity noise. Second, it cannot provide the phase relationship between individual Fourier modes, and turbulence decays downstream of the inlet plane until the near wall cycle of turbulence production has been established.

2.4 Resolution of the cavity configuration

The simulation matches one configuration of Karamcheti's experiments,[1] for a length-to-depth ratio $L/D = 3$, and a Mach number M = 0.8, with $D = 2.54$ mm as in the experiment. The computational box extends over $13D$ horizontally and $6.5D$ vertically. The slice simulated has a spanwise width of $1.6D$. The meshing is slowly nonuniform and Cartesian, with $101 \times 101 \times 101$ grid points inside the cavity and $271 \times 140 \times 101$ outside, clustered near the walls. A resolution $\Delta x_{1_{min}}^{+} \simeq 28$, $\Delta x_{2_{min}}^{+} \simeq 9$, and $\Delta x_{3}^{+} \simeq 34$ is reached. The time step is $\Delta t = 1.95 \times 10^{-8}$ s, to satisfy the CFL stability criterion with CFL = 0.66. The computation lasts 43 hours on a Nec SX-5, for 4.9 million grid-points and 70000 iterations.

The computation is initiated by extrapolating the mean inflow velocity profile into the entire computational domain. The freestream air temperature is $T_\infty = 320$ K, and the static pressure p_∞ is taken as 1 atm.

2.5 Method for extending near-field to far-field

Beyond an extrapolation surface, specified by the DNC near-field, the extrapolation method solves the isentropic Linearised Euler Equations (LEE),

$$\begin{cases} \dfrac{\partial u_i'}{\partial t} + U_0 \dfrac{\partial u_i'}{\partial x_1} + \dfrac{1}{\rho_0} \dfrac{\partial p'}{\partial x_i} = 0 \qquad i = \{1, 2, 3\} \\ \dfrac{\partial p'}{\partial t} + \rho_0 c_0^2 \dfrac{\partial u_j'}{\partial x_j} + U_0 \dfrac{\partial p'}{\partial x_1} = 0 \end{cases}$$

with $U_0 = U_\infty$ and $\rho_0 = \rho_\infty$, the freestream values from the cavity DNC. Owing to the high subsonic Mach number, M = 0.8, and the high-level pressure waves generated by the interaction with the downstream corner of the cavity, the propagation is nonlinear. To cope with this, the sound speed c_0 can vary to include a part of the eventual non linear effects on wave propagation. The first order modification from the weak shock wave theory[32] is implemented:

$$c_0 = c_\infty \left(1 + \frac{\gamma + 1}{2\gamma} \frac{p'}{p_\infty} \right)$$

This simple modification allows the inclusion of the main part of the nonlinear effects (including the $(\mathbf{u}'.\nabla)\mathbf{u}'$ term) with almost no additional cost. A better description of the

nonlinear steepening would only be possible through the use of the complete energy equation. The new set of simplified equations resolved in the acoustic part is now weakly nonlinear, and is referred to as Weakly Non Linear Euler Equations (WNLEE) in the following.

A view of the two meshgrids used for the DNC and for the WNLEE calculation is presented in figure 5. It shows the DNC region on the bottom where the full Navier-Stokes equations are solved on a non regular Cartesian grid refined near the horizontal and vertical walls of the cavity, and the acoustic region on the top where WNLEE are solved on a regular Cartesian grid. The extrapolation surface is located at $x_2 / D = 2$. In order to validate the results obtained with the extrapolation method, the region between $x_2 / D = 2$ and $x_2 / D = 5.5$ is resolved by both methods. In the DNC, radiation conditions are used for the three free-field sideview boundaries. Periodic conditions are applied for the two spanwise boundaries. In the WNLEE simulation, the same boundary conditions are used to allow a comparison with the DNC. The regular Cartesian grid in figure 5 represents the acoustic region with $181 \times 151 \times 21$ points and $\Delta x_1 = \Delta x_2 = \Delta x_3 = 0.078D$. It extends from $x_2 / D = 2$ to $x_2 / D = 13$. Its streamwise length is slightly larger than that of the DNC, from $x_1 / D = -6$ to $x_1 / D = 8$. The spanwise dimension is the same as that chosen for the DNC. For comparison, the DNC

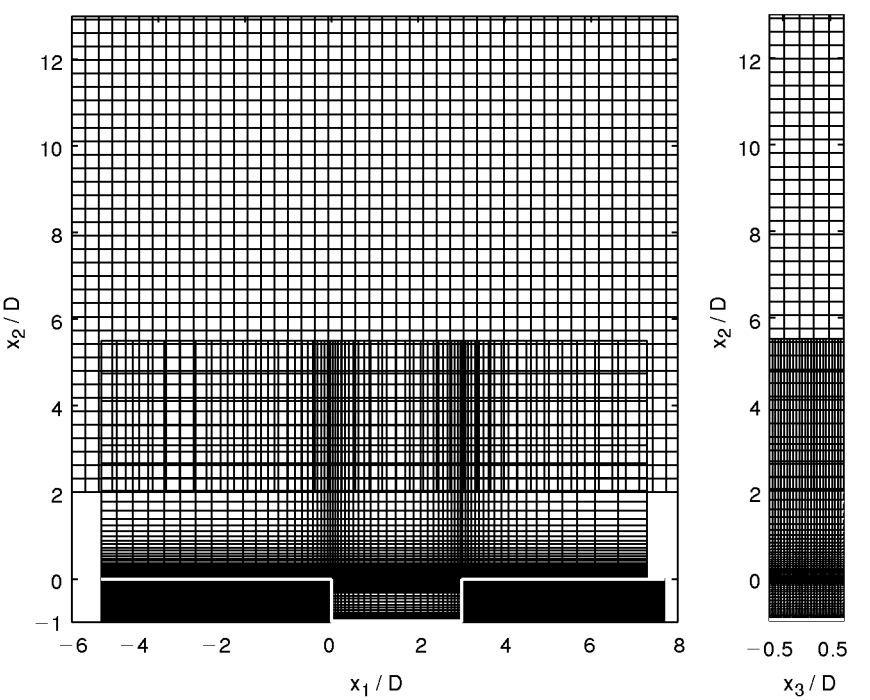

Figure 5. Superimposition of the meshgrids used for the DNC (bottom) and for the WNLEE calculation (top). The grids are shown every other four points (sideview on the left and crossview on the right).

region uses $271 \times 140 \times 101$ grid points above the cavity, and covers only $5.5D$ vertically. The refinements near the two vertical walls of the cavity, and all along the spanwise direction, needed to describe accurately the flow, induces an additional discretisation cost in the acoustic part due to the Cartesian representation. A factor of 7 can be saved with the meshgrid of the extrapolation method. In the vertical direction, the meshsize used for the WNLEE is the same as the meshsize near the extrapolation surface in the DNC. The frequency cut-off of the acoustic simulation is therefore identical to that of the DNC based on Δx_2 near $x_2 / D = 2$, thus smaller than that at the limit of the DNC domain. Moreover, the use of a regular grid minimizes the dissipation and the dispersion of the numerical schemes, which have been optimised for a constant meshsize.[22] The time step imposed by the CFL criterion is proportional to the smaller gridsize, $\Delta x_2 \simeq 0.004D$ near the walls in the DNC and $\Delta x_2 = 0.078D$ for the regular mesh. We see roughly a factor 20 decrease in computational cost. In addition, comparing the 7 spatial derivatives for the WNLEE to the 39 derivatives necessary for the Navier-Stokes solver, the computing expense is further reduced by a factor of 5.5. The WNLEE has also fewer field variables and thus smaller memory requirements. Then the global reduction of computer time is more than 700 for the extrapolation method. The WNLEE are solved with the same eleven-point stencil differencing, six substep Runge-Kutta technique, and eleven-point stencil filtering as the Navier-Stokes DNC region. The free-field boundary conditions use Tam and Dong's formulation.

3 MODE SWITCHING BETWEEN TWO CAVITY MODES

3.1 Features of the unsteady flow

The spectrum of the LES pressure fluctuations near the impingement corner is shown in figure 6(a), and exhibits two well-defined peaks. The higher frequency corresponds to a Strouhal number $\mathrm{St} = fL / U_\infty = 0.66$, and the lower frequency occurs at $\mathrm{St} = 0.33$ with a level 5 dB greater. The values measured by Karamcheti[1] for this configuration $\mathrm{St}_{\mathrm{low}} = 0.33$ and $\mathrm{St}_{\mathrm{high}} = 0.68$ are in good agreement as seen in the comparison of figure 6(b). Karamcheti observed a single peak when the incoming boundary layer was laminar with a Strouhal number $\mathrm{St} = 0.71$, slightly higher than $\mathrm{St}_{\mathrm{high}}$. The appearance of two components, for a turbulent boundary layer, was noted. The time trace of the pressure fluctuations in figure 7 is analysed to identify the portions of the signal corresponding to each frequency, and their relative amplitude. As shown in the experiments of Tang and Rockwell[33] for the impingement of a vortex upon a square corner, the impingements are characterised by a pronounced negative peak in the time traces, since the low-pressure center of the vortex arrives on the corner. The time trace is dominated by large negative peaks with a period corresponding to $\mathrm{St}_{\mathrm{low}}$. Smaller amplitude negative peaks in the middle of the low-frequency periods are also noticeable and can be attributed to the higher frequency. They are clearly visible in the cycles numbered 1 and 7 in the figure 7. They are almost undistinguishable in cycles 4 or 10, indicating a certain level of intermittency.

The cycle 6 is investigated in detail by visualizing the instantaneous vorticity and velocity at different instants, marked by the asterisk symbols in the time trace.

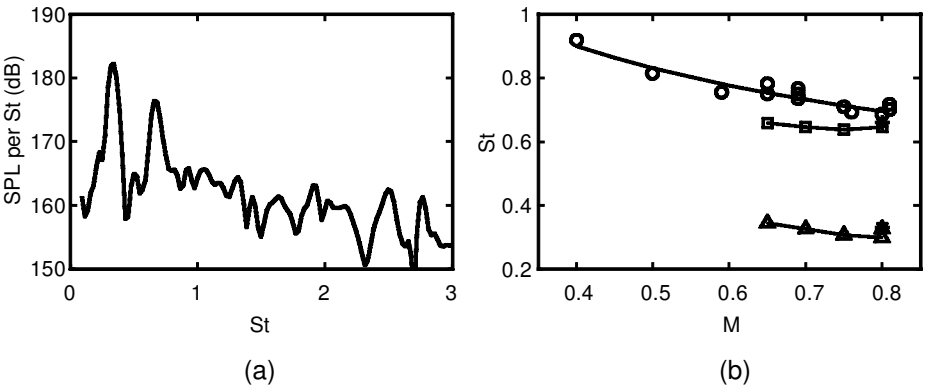

Figure 6. (a): Spectrum of the fluctuating pressure near the impingement corner at $x_1 = L$, $x_2 = 0.02D$, $x_3 = 0$; (b): Strouhal number for the principal frequencies versus the Mach number. Comparison between Karamcheti's experiments[1] ($\circ$ with laminar inflow; $\square - \Delta$ high and low components with turbulent inflow) and the present simulation ($*$) for a turbulent inflow and M = 0.8.

Three isocontours of instantaneous vorticity are superimposed on the grayscale levels representing the vorticity averaged over the spanwise homogeneous dimension, and consequently indicating the spanwise coherence of the vorticity. The first instant of figure 8 corresponds to a maximum negative value in the pressure history, and thus depicts the flowfield just after a violent impingement of a vortex on the downstream corner. The vorticity isocontours show that this is not a single vortex but rather a cluster of small scales. This structure is clipped as it impinges. One part is ejected in the reattached boundary layer, and the other part travels down along the vertical wall, then upstream along the cavity floor. The resulting wall jet-like flow is clearly apparent in

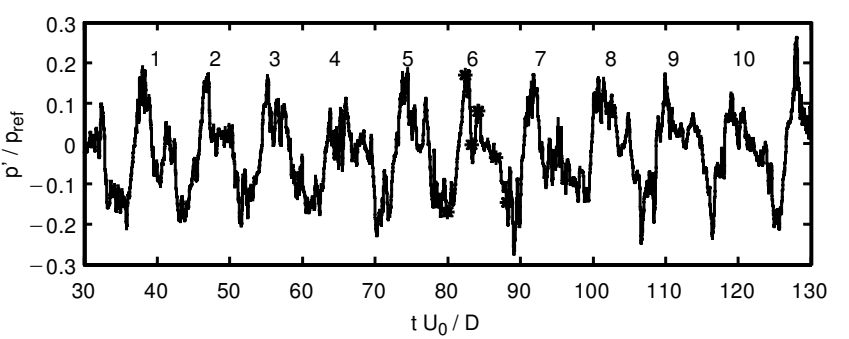

Figure 7. Time trace of the fluctuating pressure near the impingement corner at $x_1 = L$, $x_2 = 0.02D$, $x_3 = 0$.

the corresponding plot of velocity vectors in the midplane of the cavity. The velocity field near the impingement corner exhibits a violent ejection of fluid from the cavity. A strongly coherent roll, shed from the leading edge, is located in the middle of the shear layer. In figure 8(b), this incident structure is located just upstream of the downstream corner, and another roll has been shed in the shear layer, giving an instantaneous view with two coherent Kelvin-Helmholtz vortices in the shear layer. Therefore this is a mode II of cavity oscillations. The instantaneous pressure reaches its maximum value, and the velocity field in the vicinity of the impingement corner shows a downward deflection, and the formation of the jet-like flow along the vertical wall. The next frame (fig. 8(c)) corresponds to a relative negative peak in the pressure time trace, and depicts the impingement of the cluster of vorticity of the previous picture. Its center is nearly coincident with the cavity corner. An upward-oriented outflow from the cavity is induced in the velocity field. A rising of the entire shear layer is visible. Consequently, the shear layer in the next picture (fig. 8(d)) is formed by only one coherent roll extending from the bottom of the cavity to the edge of the shear layer. This is a mode I of cavity oscillations. The last third of the flow within the cavity is included in the large-scale swirl pattern, so that the recirculation bubble occupying the two last thirds of the cavity in the previous images is now separated in two parts. The next picture shows this large-scale cluster of vorticity approaching the downstream corner, drawing along an important part of the flow within the cavity. A new intense roll is shed at the leading edge. The last view in figure 8(f) is similar to the first one and corresponds to a negative pressure peak. In this case, the fluid ejected out of the cavity is drawn upward by the rotation of the large-scale cluster as it encounters the corner.

The interesting feature in the preceding views is the alternance between two instantaneous sizes of the dominant structures in the shear layer. It is well known that the number of vortices between the two corners of the cavity corresponds to the Rossiter mode number. The instantaneous views therefore provide evidence on a switching between modes I and II, associated respectively to the lower and higher frequencies in the spectra. Cattafesta *et al.*[7] investigated this phenomenon by using Schlieren photographies for a turbulent cavity flow ($L/D = 2$, $\mathrm{M} = 0.4$, $\mathrm{Re} = 2.5 \times 10^6$). These authors provide pictures of the shear layer, showing that the size of the dominant structures can change with time, and that switching between modes I, II and III can occur. Comparison with the cinema PIV sequence of Lin and Rockwell,[34] for a $L/D = 2$ cavity in a 12 cm/s water flow, and with an incoming boundary layer having roughly the same Reynolds number based on the momentum thickness, $\mathrm{Re}_{\delta_\theta} \simeq 1400$, as in the present simulation, displays a lot of similarities. Lin and Rockwell's time trace near the impingement corner also indicates substantial modulation between a low and a high component. The instantaneous PIV images depict remarkably similar features for the shear layer behaviour as well as for the velocity pattern inside the cavity. However, Lin and Rockwell's interpretation of these low and high oscillation frequencies is slightly different. In their case, the high frequency is dominant and is called the fundamental, whereas the low component is considered as a subharmonic. The origin of this subharmonic may be associated with a modulation of the shear layer trajectory by the recirculating flow within the cavity.

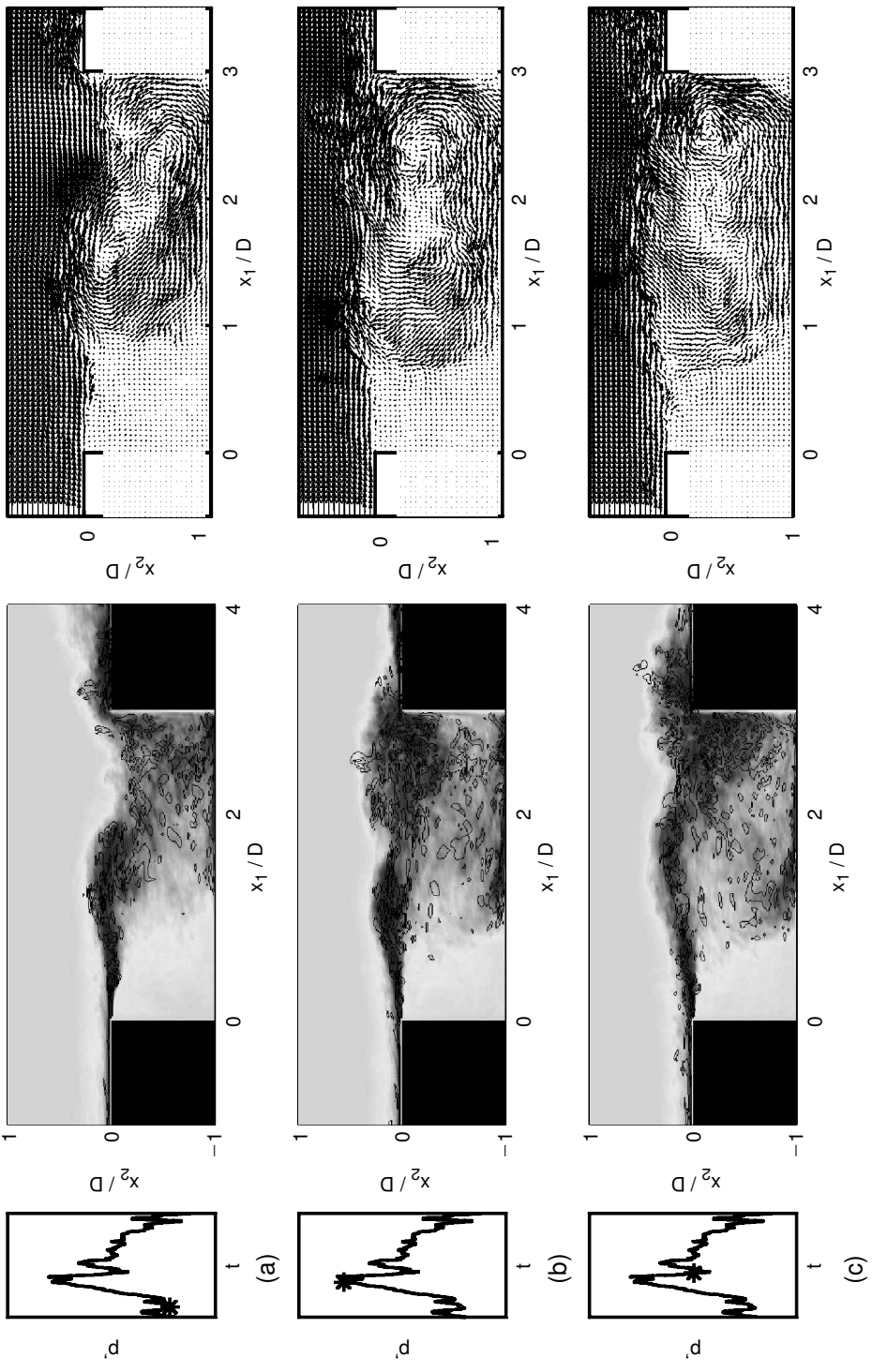
p'
t
(a)
(b)
(c)
x2 / D
x1 / D

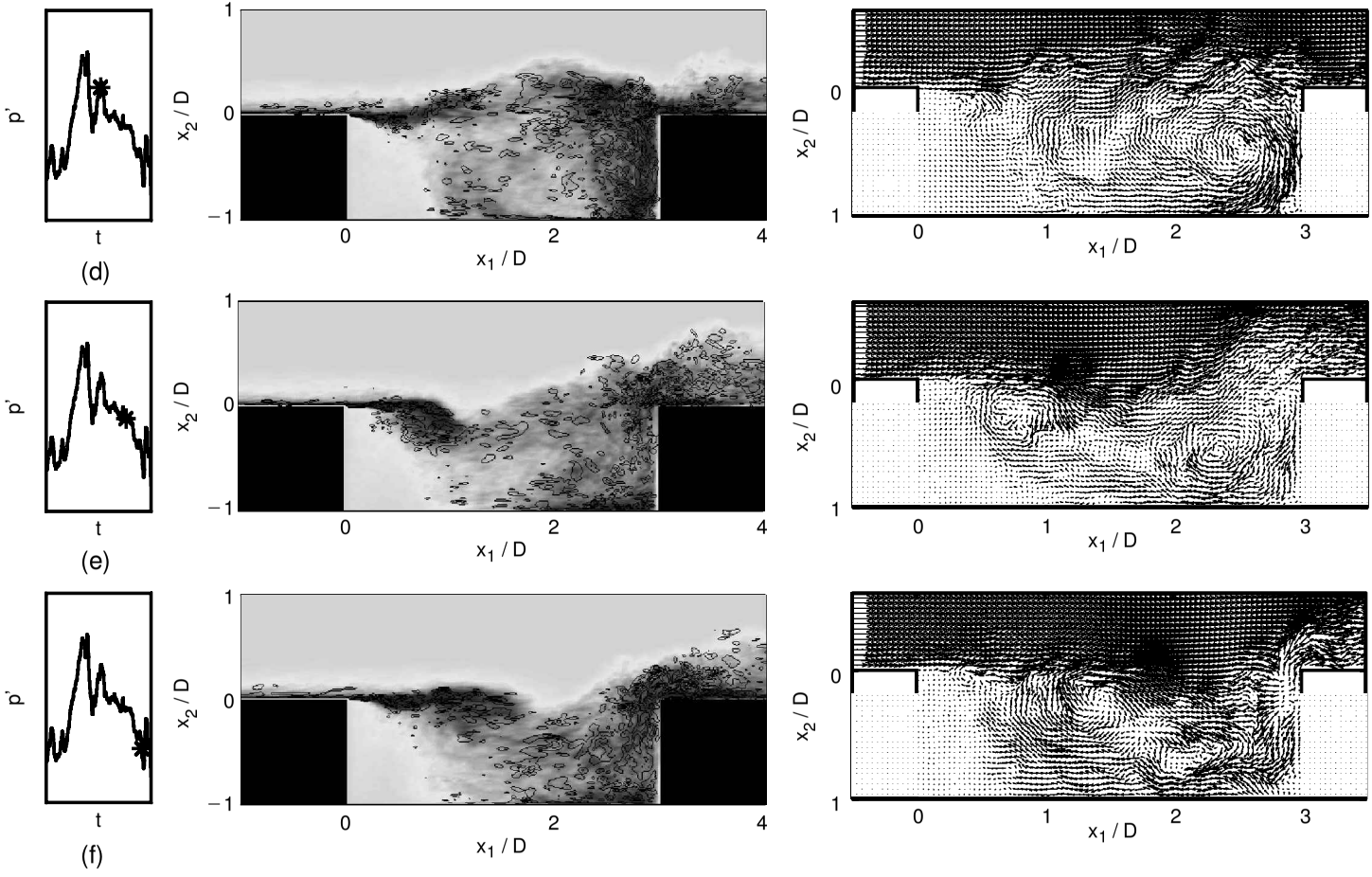

Figure 8. Snapshots of vorticity and velocity during cycle 6. The asterisks indicate the instants in the pressure time trace on the left. In the middle, 3 isocontours of instantaneous modulus $\|\omega\|$ of vorticity (1, 2 and $3 \times 10^6 s^{-1}$ are superimposed on the instantaneous vorticity averaged over the spanwise direction (grayscale between -1.2 and $1.2 \times 10^6 s^{-1}$). On the right, distributions of velocity vectors are plotted after interpolation on a regular grid.

3.2 Selection of the shear layer instabilities

In order to examine the growth of the shear layer between the two corners of the cavity, figure 9(a) shows the evolution of the momentum thickness defined as:

$$\delta_\theta = \int_{-\infty}^{+\infty} \frac{\overline{u}_1}{U_\infty}\left(1 - \frac{\overline{u}_1}{U_\infty}\right) dx_2$$

normalised by the reference momentum thickness at the upstream edge, $\delta_{\theta_R} = 8.86 \times 10^{-5}$m. For this location, a shape factor $H = 1.44$ is found, and the Reynolds number based on the momentum thichness is $\mathrm{Re}_{\delta_\theta} = 1695$. The momentum thickness growth is linear by parts and three regions can be distinguished: the first between $x_1/L = 0$ and 0.45 with a growing rate $d\delta_\theta / dx_1 \simeq 0.05$, the second between $x_1/L = 0.45$ and 0.75 with $d\delta_\theta / dx_1 \simeq 0.01$. The third region extends between $x_1/L = 0.75$ and 0.9 with $d\delta_\theta / dx_1 \simeq 0.06$. A similar distribution has been observed experimentally by Oster and Wygnanski[35] for a forced mixing layer. The first region with a high spreading rate corresponds to the formation of large-scale Kelvin-Helmholtz vortices at the frequency of the excitation, provided here by the intense acoustic field. When this frequency is much lower than the natural most instable frequency of the shear layer determined by the linear theory of stability of parallel flows, the small-scale vortices shed at the instability frequency ($St_{\delta_\theta} = 0.017$) interact together to form a large-scale roll whose wavelength is that of the low-frequency forcing.

Figure 9(b) displays the early development of the shear layer. The low-frequency component forces the shear layer to undulate, and the vortices, shedded at the initial instability frequency, are displaced laterally. Owing to their induced field, the vortices are drawn together and coalesce into a large vortex. The simultaneous coalescence of a number of vortices, referred to as collective interaction by Ho et Nosseir[36] participates in the selection of the well-defined frequencies, characteristic of flow with self-sustained oscillations. The necessary condition for this interaction is a high-amplitude low-frequency excitation. The two principal consequences are the drop in passage frequency and a high spreading rate for the shear layer.

In the second region, the growth is very slight since the shear layer experiences no pairing event. The vortices grow only thanks to viscous spreading and entrainment of the surrounding fluid. The last region is mainly influenced by the impingement process. The inflow-outflow motion near the downstream corner induces a subsequent vertical velocity which contributes to the high spreading rate.

3.3 Turbulence intensities

Visualizations of the turbulence intensities are plotted in the figure 10. The maximum amplitude of the normalised *rms* velocity components are respectively 0.34, 0.26, and 0.19, for the longitudinal, crossflow and transverse components. The distribution of u_{rms} shows that the highest levels are found in the early development of the shear layer where small-scale vortices are shed from the leading edge. Another high-level regions are found in front of the downstream vertical wall and at the bottom of the cavity near

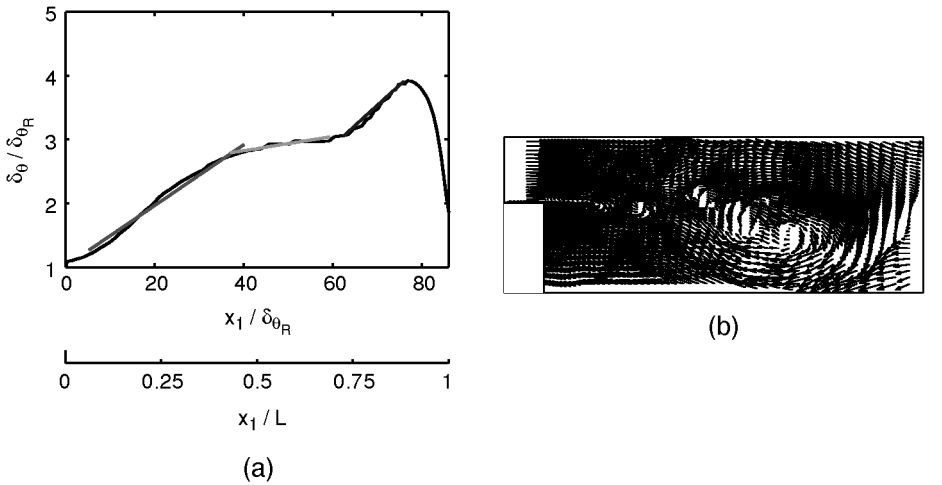

Figure 9. (a): Non-dimensional momentum thickness $\delta_\theta / \delta_{\theta_R}$ between the two corners of the cavity; (b): Zoom of velocity field around the upstream corner ofthe cavity $(-0.1 < x_1 / D < 1.1)$ showing the collective interaction.

the middle. These two regions mark the beginning and the end of the reverse jet-like flow in the cavity.

The quantities v_{rms} and w_{rms} are maximum near the downstream corner due to the impingement process. The high-amplitude region begins after a distance of $0.5D$ from the leading egde and encompass all the vertical extent further downstream. The principal information from these turbulence intensities is the great unsteadiness of the flow within the cavity, which seems severely coupled to the shear layer. The velocity stress tensor uv_{rms} distribution shows high correlation in the shear layer due to the existence of small-scale structures especially during the first half of its growth. The peak value of 0.04 compares well with the measurements of Oster and Wygnanski[35] (0.036) for a turbulent mixing layer. This is however greater than the values of Lin and Rockwell[34] (0.01) or Forestier[11] (0.023) for cavity flows. This overestimation may be associated to the too dissipative effect of the eddy viscosity model in the separated shear layer and needs further investigation. The interaction with the downstream is marked by the change of the sign of the stress tensor due to the presence of an important vertical motion.

3.4 Role of the recirculation

Figure 11 shows the velocity vectors associated with the mean velocity in the midplane of the cavity. A downward deflected flow forms a jet that continues along the bottom of the cavity and is lastly drawn upward toward the separating shear layer at the upstream corner to satisfy entrainment demands.The last two thirds of the cavity exhibit a large-scale recirculation bubble, also visible in the instantaneous velocity pictures of figure 8. The averaged pattern is in agreement with the features of the PIV

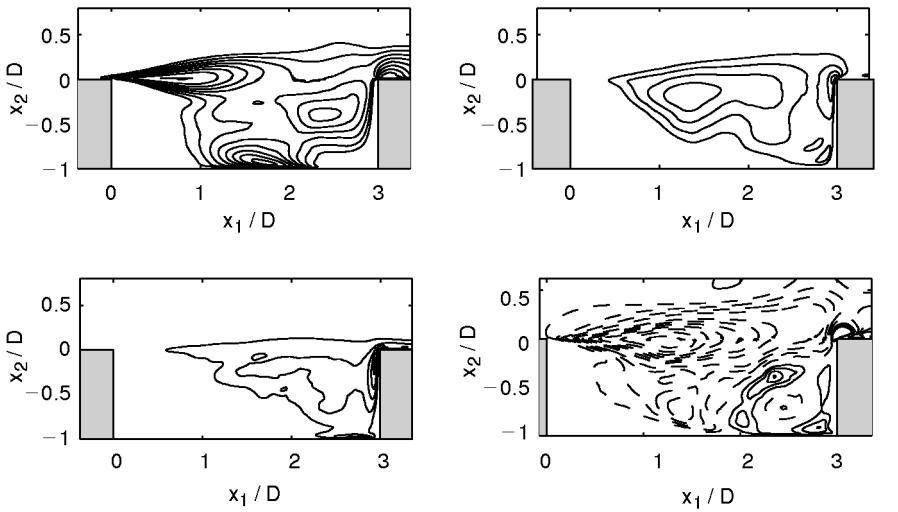

Figure 10. Contours for the turbulent intensities: from left to right, and from top to bottom, $u_{rms} = \sqrt{\overline{u_1'^2}} / U_\infty$ (8 isocontours between 0.12 and 0.26 with interval 0.02), $v_{rms} = \sqrt{\overline{u_2'^2}} / U_\infty$ (6 isocontours between 0.12 and 0.22 with interval 0.02), $w_{rms} = \sqrt{\overline{u_3'^2}} / U_\infty$ (6 isocontours between 0.12 and 0.22 with interval 0.02), $uv_{rms} = \overline{u_1' u_2'} / U_\infty^2$, (– – –) 12 negative isocontours between −0.024 and -0.002 with interval 0.002), (——) 4 positive isocontours between 0.001 and 0.004 with interval 0.001).

measurements of Lin and Rockwell, where the recirculation occupies the right half of the cavity with an aspect ratio L/D of 2. The upward entrainment flow may influence the initial development of the shear layer. Lin and Rockwell suggest that the unsteadiness of this upward-oriented jet contributes to the modulated character of the separated shear layer, and thus to the appearance of a low-frequency peak in the pressure spectra near impingement. Similarly, the views of figure 8 indicate that a number of admissible patterns of the recirculation can occur. In figure 8(d)(e) the swirl pattern encompasses one half of the recirculation, suggesting the possibility of a coupling of the recirculation with the separated shear layer. Recent bidimensional simulations of Pereira and Sousa[37] and Najm and Ghoniem[38] address the potential role of the large-scale vortex within the cavity. By viewing this region of the flow as a dynamical system, it is possible to define a mechanism of instability due to the recirculation system.

We must notice that the oscillation components having frequencies lower than the fundamental have been found in the spectra of velocity fluctuations in mixing layer-edge (Hussain and Zaman[39]), cavity (Rockwell and Knisely[40,41]), and jet-edge interactions (Stegen and Karamcheti[42]), suggesting that there is a well-defined mechanism for generating these components, common to a number of flow geometries.

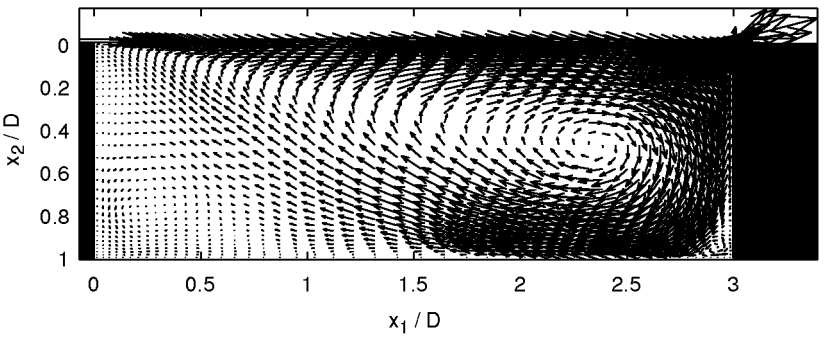

Figure 11. Distribution of averaged velocity inside the cavity in the median plane.

Noting that mixing layer-edge or jet-edge configurations do not involve a recirculating flow, we can conclude that the recirculating flow is not necessary to induce a modulation of the shear layer.

3.5 Features of the radiated acoustic field

The pressure field obtained directly by DNC is plotted in figure 12(a). It shows a strong downstream directivity due to the convection of acoustic wave fronts by the mean flow combined with the reflections on the cavity walls. The dominant frequency corresponds to St_{low}. The pressure spectrum in the near-field (fig. 12(b)) exhibits a low-frequency peak 12 dB higher than the high-frequency peak. Note that the Schlieren visualization of Karamcheti for this configuration indicates the predominance of the high component. In the present simulation, the predominance of the lower mode in the shear layer probably related to the dissipative effect of the viscosity model implies a more violent impingement of the larger-scale structures upon the downstream corner of the cavity, so that the lower component is reinforced in the acoustic spectra.

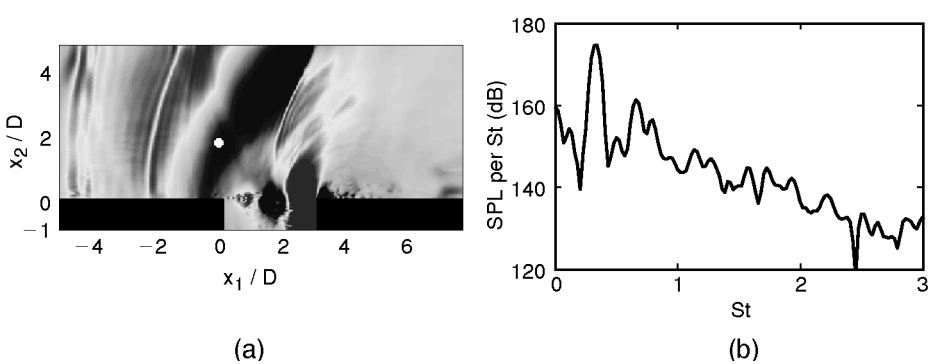

Figure 12. (a) Pressure field from the DNC in the midplane of the cavity (levels between −5000 and 5000 Pa); (b) Spectrum of pressure fluctuations at the location indicated by a bullet on the left.

The far-field radiation computed by the extrapolation method is presented in figure 13(a). The extrapolation method is seen to extend well the DNC solution. The profiles in the overlapping region, shown in figure 13(b), are in good agreement with the DNC profiles. The proposed method would be most useful when a large amount of sound field data are needed at not too large distance from the source. For a very long-range propagation, integral methods may still be preferable. In the present application with a high subsonic flow (M = 0.8), the non linear steepening of the wavefronts imposed a relatively fine meshsize to reduce numerical oscillations. For lower Mach number, the wavelengths involved are larger and the propagation would remain linear, so that the difference between the meshsizes for the acoustic calculation and for the DNC would be increased.

4. CONCLUSION

The interaction of a turbulent boundary layer with a cavity, and its radiated field are computed using Direct Noise Computation. The reproduction of a configuration investigated experimentally by Karamcheti is performed using Large Eddy Simulation to maintain reasonable computational cost. The bypass transition toward realistic turbulence ahead of the cavity is successfully achieved through the superimposition of random Fourier modes on a turbulent mean profile. A method for extending the acoustic near-field to far-field is presented: WNLEE are solved to extent the DNC solution, reducing the cost of the calculation but maintaining a high accuracy.

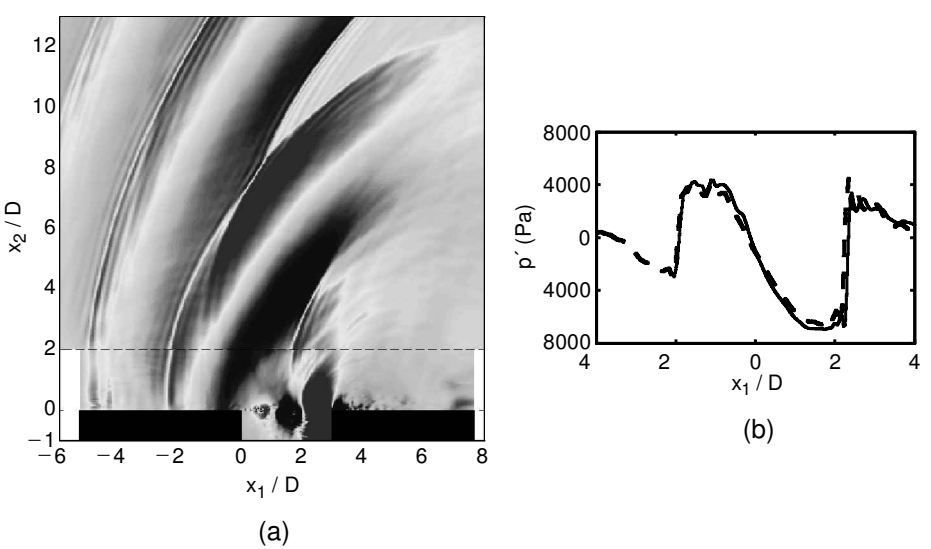

Figure 13. **(a)**: Pressure field obtained by the extrapolation method from the extrapolation surface (shown by the dashed line). The DNC near-field is plotted under the extrapolation surface. Sideview in the median plane. Levels between −5000 and 5000 Pa; (**b**): Longitudinal pressure profiles along $x_2 \simeq 3.6D$. (——), DNC and (– – –), WNLEE.

The principal observation concerning cavity noise is the possibility of switching between mode I and mode II of cavity oscillations. This switching is not random in time but follows a cycling pattern, with a successive alternance between the two modes, even if a certain level of intermittency is observed in this succession. In turbulent conditions, the coherent structures adopt the shape of clusters of small scales, and the alternance of different size of the dominant structures proceed by a reorganisation of these clusters. The examination of the early shear-layer growth reveals that the formation of large-scale structures is possible through a collective interaction after the upstream corner, corresponding to the fusion of a number of smaller vortices shedded at the most instable frequency of the shear-layer. This phenomenon appears to be of fundamental interest in the process of selection of the main oscillation frequencies. Another interesting finding is the strong unsteadiness of the recirculating flow within the cavity, which seems severely coupled to the shear-layer modulations. However the role of the recirculating flow on the switching phenomenon is not clear since the coexistence of different modes has been noticed in the self-sustained oscillations for configurations without adjacent recirculating flows. The acoustic near-field obtained by the DNC is extended to the far-field by using simplified equations for the acoustic disturbances, and clearly indicate the predominance of the lower component. In the present simulation, the development of the lower mode is promoted by the numerics, so that a more violent impingement upon the downstream corner of the cavity is induced and will dominate the acoustic radiation.

ACKNOWLEDGMENTS

Supercomputer time is supplied by Institut du Développement et des Ressources en Informatique Scientifique (IDRIS - CNRS).

REFERENCES

1. Karamcheti, K., Acoustic radiation from two-dimensional rectangular cutouts in aerodynamic surfaces. *NACA Technical Note 3487*, 1955.
2. Colonius, T., Basu, A.J. & Rowley, C.W., Numerical investigation of the flow past a cavity, *AIAA Paper 99-1912*, 1999.
3. Shieh, C.M. & Morris, P.J., Parallel computational aeroacoustic simulation of turbulent subsonic cavity flow, *AIAA Paper 2000-1914*, 2000.
4. Heo, D.N. & Lee, D.J., Numerical investigation of the cover-plates effects on the rectangular open cavity, *AIAA Paper 2001-2127*, 2001.
5. Gloerfelt, X., Bailly, C. & Juvé, D., Computation of the noise radiated by a subsonic cavity using direct simulation and acoustic analogy, *AIAA Paper 2001-2226*, 2001.
6. Rockwell, D., Oscillations of impinging shear layers, *AIAA Journal*, 1983, 21(5), p. 645–664.
7. Cattasfesta III, L.N., Garg, S., Kegerise, M.A. & Jones, G.S., Experiments on compressible flow-induced cavity oscillations, *AIAA Paper 98-2912*, 1998.

8. Gloerfelt, X., Bailly, C. & Juvé, D., Direct computation of the noise radiated by a subsonic cavity flow and application of integral methods, *Journal of Sound and Vibration*, 2003, 226(1), p. 119–146.
9. Larchevêque, L., Sagaut, P., Mary, I., Labbé, O. & Comte, P., Large-eddy simulation of a compressible flow past a deep cavity, *Physics of Fluids*, 2003, 15(1), p. 193–210.
10. Gloerfelt, X., Bogey, C., Bailly, C. & Juvé, D., Aerodynamic noise induced by laminar and turbulent boundary layers over rectangular cavities, *AIAA Paper 2002-2476*, 2002.
11. Forestier, N., Jacquin, L. & Geffroy, P., The mixing layer over a deep cavity at high-subsonic speed, *Journal of Fluid Mechanics*, 2003, 475, p. 101–145.
12. Shieh, C.M. & Morris, P.J., Comparison of two- and three-dimensional turbulent cavity flows, *AIAA Paper 2001-0511*, 2001.
13. Fureby, C. & Grinstein, F.F., Large Eddy Simulation of high-Reynolds number free and wall-bounded flows, *Journal of Compututational Physics*, 2002, 181, p. 68–97.
14. Ahuja, K.K. & Mendoza, J., Effects of cavity dimensions, boundary layer, and temperature in cavity noise with emphasis on benchmark data to validate computational aeroacoustic codes, *NASA CR-4653*, 1995.
15. Pilon, A.R. & Lyrintzis, A.S., Refraction corrections for the Kirchhoff method, *AIAA Paper 97-1654*, 1997.
16. Shih, S.H., Hixon, D.R., Mankbadi, R.R., Pilon, A. & Lyrintzis, A., Evaluation of far-field jet noise prediction methods, *AIAA Paper 97-0282*, 1997.
17. Freund , J.B., Lele , S.K. & Moin , P., Matching of near/far-field equation sets for direct computations of aerodynamic sound, *AIAA Paper 93-4326*, 1993.
18. Shih, S.H., Hixon, D.R. & Mankbadi, R.R., A zonal approach for prediction of jet noise, *AIAA Paper 95-144*, 1995.
19. Deardorff, J.W., A numerical study of three-dimensional turbulent channel flow at large Reynolds numbers, *Journal of Fluid Mechanics*, 1970, 41(2), p. 453–480.
20. Erlebacher, G., Hussaini, M.Y., Speziale, C.G. & Zang, T.A., Toward the large-eddy simulation of compressible turbulent flows, *Journal of Fluid Mechanics*, 1992, 238, p. 155–185.
21. Moin, P. & Kim, J., Numerical investigation of turbulent channel flow, *Journal of Fluid Mechanics*, 1982, 118, p. 341–377.
22. Bogey, C. & Bailly, C., A family of low dispersive and low dissipative explicit schemes for computing aerodynamic noise, *AIAA Paper 2002-2509*, 2002.
23. Bogey, C. & Bailly, C., Three-dimensional non-reflective boundary conditions for acoustic simulations: far field formulation and validation test cases, *Acta Acustica*, 2002, 88, p. 463–471.
24. Tam, C.K.W. & Dong, Z., Advances in numerical boundary conditions for computational aeroacoustics, *Journal of Computational Acoustics*, 1999, 6(4), p. 377–402 (or AIAA Paper 97-1774).

25. Rai, M.M. & Moin, P., Direct numerical simulation of transition and turbulence in a spatially evolving boundary layer, *Journal of Computational Physics*, 1993, 109, p. 169–192.
26. Ducros, F., Comte, P. & Lesieur, M., Large-eddy simulation of transition to turbulence in a boundary layer developing spatially over a flat plate, *Journal of Fluid Mechanics*, 1996, 326, p. 1–36.
27. Voke, P.R. & Yang, Z., Numerical study of bypass transition, *Physics of Fluids*, 1995, 7(9), p. 2256–2264.
28. Bailly, C., Lafon, P. & Candel, S., A stochastic approach to compute noise generation and radiation of free turbulent flows, *AIAA Paper 95-092*, 1995.
29. Spalart, P.R., Direct simulation of a turbulent boundary layer up to $\mathrm{Re}_{\delta_\theta} = 1410$, *Journal of Fluid Mechanics*, 1988, 187, p. 61–98.
30. Head, M.R. & Bandyopadhyay, P., New aspects of turbulent boundary layer structures, *Journal of Fluid Mechanics*, 1981, 107, p. 297–338.
31. Bogey, C. & Bailly, C., LES of a high Reynolds, high subsonic jet: Effects of the subgrid modellings on flow and noise, *AIAA Paper 2003-3557*, 2003.
32. Whitham, G.B., *Linear and nonlinear waves*, Wiley, New York, 1974, p. 312–338.
33. Tang, Y.-P. & Rockwell, D., Instantaneous pressure fields at a corner associated with vortex impingement, *Journal of Fluid Mechanics*, 1983, 126, p. 187–204.
34. Lin, J.C. & Rockwell, D., Organized oscillations of initially turbulent flow past a cavity, *AIAA Journal*, 2001, 39(6), p. 1139–1151.
35. Oster, D. & Wygnanski, I., The forced mixing layer between parallel streams, *Journal of Fluid Mechanics*, 1982, 123, p. 91–130.
36. Ho, C.-M. & Nosseir, N.S., Dynamics of an impinging jet. Part 1. The feedback phenomenon, *Journal of Fluid Mechanics*, 1981, 105, p. 119–142.
37. Pereira, J.C.F. & Sousa, J.M.M., Experimental and numerical investigation of flow oscillations in a rectangular cavity, *ASME Journal of Fluids Engineering*, 1995, 117, p. 68–74.
38. Najm, H.N. & Ghoniem, A.F., Numerical simulation of the convective instability in a dump combustor, *AIAA Journal*, 1991, 29(6), p. 911–919.
39. Hussain, A.K.M.F. & Zaman, K.B.M.Q., The free shear layer tone phenomenon and probe interference, *Journal of Fluid Mechanics*, 1978, 87(2), p. 349–383.
40. Rockwell, D. & Knisely, C., Vortex-edge interaction: Mechanisms for generating low frequency components, *Physics of Fluids*, 1980, 23(2), p. 239–240.
41. Knisely, C. & Rockwell, D., Self-sustained low frequency components in an impinging shear layer, *Journal of Fluid Mechanics*, 1982, 116, p. 157–186.
42. Stegen, G.R. & Karamcheti, K., Multiple tone operation of edgetones, *Journal of Sound and Vibration*, 1970, 12(3), p. 281–284.